Influence of complex driving motion on propulsion performance of a heaving flexible foil

Chenglei Wang & Hui Tang*

Department of Mechanical Engineering,

The Hong Kong Polytechnic University, Kowloon, Hong Kong SAR, China

Correspondence to: h.tang@polyu.edu.hk

Abstract

This study explores the effects of complex driving motion on the propulsion performance of a flexible foil heaving in the flight regimes of natural flyers. Such a fluid-structure interaction problem is numerically studied using an immersed boundary lattice Boltzmann method (IBLBM) based numerical framework. It is found that, at the Reynolds number 200 and when the foil's bending stiffness and mass ratio are moderate, adding an extra driving motion of doubled frequency to a purely harmonic motion on the foil's leading edge can enhance the thrust and propulsive efficiency by about 860% and 70%, respectively. The improvement in thrust increases with the extra-driving-motion amplitude. When the extra-driving-motion amplitude is fixed, there exists an optimal extra-driving-motion phase angle. As the foil becomes much stiffer or lighter, the improvement in the propulsion performance turns less. On the other hand, as the foil becomes much more flexible or heavier, drag instead of thrust is generated, and extra driving motion brings no improvement. Although the extra driving motion can improve the foil's propulsion performance in flows of different Reynolds numbers, the increasing rate of the thrust reduces with the Reynolds number. Through this study, details about the competitions among various forces exerted on the foil and their roles in the foil's dynamics are also revealed.

Keywords: propulsion enhancement, heaving flexible foil, complex driving motion

1 Introduction

As one of the most sophisticated lift/thrust generation methods found in nature, the flapping motion adopted by birds and insects can provide superior maneuverability and locomotor performance for low-Reynolds-number flights [1]. In recent years numerous studies have been conducted to reveal the fundamental mechanisms of lift/thrust generation by flapping wings [2, 3], or to explore the influence of a series of key parameters, such as the Strouhal number [4, 5, 6, 7], reduced frequency [4, 5], Reynolds number [8], aspect ratio [9], flexibility [10, 11] and mass ratio [10, 11, 12], on flapping-wing aerodynamics. On these topics Shyy et al.[1, 13, 14] have given several comprehensive reviews.

In many existing investigations, for simplification the flapping of natural flyers was commonly assumed as a harmonic motion realized at a single frequency [10, 12, 15]. However, as the output of a typical neural control system [16, 17], it is usually not the case, as evidenced in Willmott and Ellington [18] and Altshuler et al. [19]. To facilitate more realistic flapping motions, therefore, in some studies wing kinematics was first recorded and measured from natural flyers, and then applied in the following experiments/simulations, such as in Aono et al.[20], Liu [21] and Bomphrey et al. [22].

From a signal-processing point of view, a real flapping motion consists of a number of harmonic motions operating at various frequencies, i.e., a combination of a base motion at a fundamental frequency and multiple extra driving motions at other frequencies. Hence, the major difference in the wing kinematics of the simplified and real flapping motions in literature is the extra driving motion. Nevertheless, the role played by the extra driving motion on the aerodynamic performance of natural flyers has rarely been explored. Thus far, only Lehn et al. [17] have experimentally proved that undulatory swimmers can utilize extra driving motion to positively alter boundary-layer vortices so as to enhance their propulsion performance. However, this finding from undulatory swimmers may not be applicable to natural flyers, since several key dimensionless parameters, such as the mass ratio and the dimensionless heaving frequency, in these two flapping phenomena fall into quite different ranges. Thus, the influence of extra driving motion on the aerodynamic performance of natural flyers still remains unclear. To bridge this knowledge gap, this paper aims to investigate the effect of extra driving motion on the propulsion performance of a flexible foil heaving heaving in the flight regimes of natural flyers. Such a fluid-structure interaction problem is numerically studied using an immersed boundary lattice Boltzmann method (IBLBM) based framework.

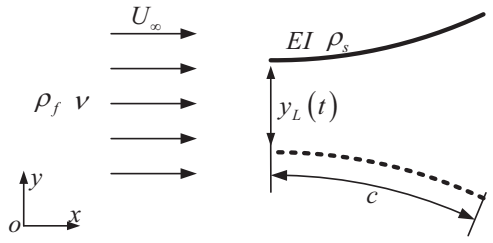

Figure 1: Schematic of a flexible foil undergoing a pure heaving motion $y_L(t)$ prescribed by Equation 1. U_∞ is the freestream velocity, ρ_f the fluid density, ν the fluid kinematic viscosity, EI the foil's bending stiffness, ρ_s the foil's linear mass density, and c the chord length.

The remaining of this paper is organized as follows. The problem setup and numerical method are described in Section 2. The influence of extra driving motion on the aerodynamic performance of a foil with different bending stiffness and mass ratios heaving at two Reynolds numbers is examined and discussed in Section 3. A conclusion is given in Section 4.

2 Problem description and methodology

2.1 Problem description

In this study, a two-dimensional thin foil with chord length c, bending stiffness EI and linear density ρ_s is immersed in a uniform incoming flow with velocity U_∞, density ρ_f and kinematic viscosity ν, as depicted in Figure 1. A harmonically heaving motion with frequency f_b and amplitude h_b (defined as the base motion) is imposed at the foil's leading edge, which is overlaid by another harmonic driving motion with higher frequency f_e, generally smaller amplitude h_e and relative phase angle ϕ_e. Such a combined heaving motion can be described as

$$y_L(t) = \frac{h_b}{2}\cos(2\pi f_b t) + \frac{h_e}{2}\cos(2\pi f_e t + \phi_e) \tag{1}$$

where y_L is the leading edge's y displacement, and the subscripts "b" and "e" denote the base and extra-driving-motion parameters, respectively.

Assuming the foil as a clamped-free, inextensible elastic plate, its dynamics is governed by two nonlinear equations [23]

$$\rho_s \frac{\partial^2 \boldsymbol{X}}{\partial t^2} - \frac{\partial}{\partial s}\left(T\frac{\partial \boldsymbol{X}}{\partial s}\right) + \frac{\partial^2}{\partial s^2}\left(EI\frac{\partial^2 \boldsymbol{X}}{\partial s^2}\right) = \boldsymbol{F}_f \tag{2}$$

$$\frac{\partial \boldsymbol{X}}{\partial s}\cdot\frac{\partial \boldsymbol{X}}{\partial s} = 1 \tag{3}$$

with boundary conditions

$$y(t,0) = y_L(t); \frac{\partial \boldsymbol{X}}{\partial s}(t,0) = (1,0) \qquad \text{imposed at the leading edge,}$$

and $$T(t,c) = 0; \frac{\partial^2 \boldsymbol{X}}{\partial s^2}(t,c) = \frac{\partial^3 \boldsymbol{X}}{\partial s^3}(t,c) = (0,0) \qquad \text{imposed at the trailing edge,}$$

where s is the Lagrangian coordinate along the foil, $\boldsymbol{X}$ the foil's position, T the tension force serving to satisfy the inextensible condition [23], and $\boldsymbol{F}_f$ the fluid loading acting on the flexible foil, i.e., the difference in flow-induced stress between the upper and lower surfaces of the foil at $\boldsymbol{X}$.

The flow dynamics can be described by the incompressible Navier-Stokes equations

$$\frac{\partial \boldsymbol{v}}{\partial t} + \boldsymbol{v} \cdot \nabla \boldsymbol{v} = -\frac{1}{\rho_f} \nabla p + \nu \nabla^2 \boldsymbol{v} + \boldsymbol{f}_e \tag{4}$$

$$\nabla \cdot \boldsymbol{v} = 0 \tag{5}$$

where $\boldsymbol{v}$ is the flow velocity, p the pressure, ∇ the gradient operator, and $\boldsymbol{f}_E$ the external force.

To parameterize this fluid-structure system, the freestream velocity (U_∞), chord length (c), fluid density (ρ_f) and base-motion frequency (f_b) are chosen as reference variables. Equations 1 to 5 can be non-dimensionalized as

$$y_L^*(t^*) = \frac{h_b^*}{2} \cos(2\pi t^*) + \frac{h_e^*}{2} \cos(2\pi f_e^* t^* + \phi_e) \tag{6}$$

$$\frac{m^* k^2}{\pi^2} \frac{\partial^2 \boldsymbol{X}^*}{\partial t^{*2}} - \frac{\partial}{\partial s^*} \left(T^* \frac{\partial \boldsymbol{X}^*}{\partial s^*} \right) + \frac{\partial^2}{\partial s^{*2}} \left(E I^* \frac{\partial^2 \boldsymbol{X}^*}{\partial s^{*2}} \right) = \boldsymbol{F}_f^* \tag{7}$$

$$\frac{\partial \boldsymbol{X}^*}{\partial s^*} \cdot \frac{\partial \boldsymbol{X}^*}{\partial s^*} = 1 \tag{8}$$

$$\frac{k}{\pi} \frac{\partial \boldsymbol{v}^*}{\partial t^*} + \boldsymbol{v}^* \cdot \nabla^* \boldsymbol{v}^* = -\nabla^* p^* + \frac{1}{\mathrm{Re}} \nabla^{*2} \boldsymbol{v}^* + \boldsymbol{f}_E^* \tag{9}$$

$$\nabla^* \cdot \boldsymbol{v}^* = 0 \tag{10}$$

For ease of reference, the definitions of all the dimensionless parameters in Equations 6 to 10 are elaborated in Table 1, where the symbol "-" in the third column indicates that the corresponding parameter changes with time and hence is updated during the simulation.

Table 1 also lists another two key independent parameters, i.e., the Strouhal number (St) and the dimensionless base-motion frequency (f_b^*). St in conjunction with the reduced frequency k determines the base-motion amplitude h_b^*. It reflects the ratio of the heaving speed to the forward speed, thus characterizes the vortex dynamics and vortex shedding behaviour [10]. Typically, St adopted by natural flyers varies from 0.2 to 0.4 [14], thus it is set as 0.3 in the present study. f_b^* represents the ratio between the foil's effective inertia (defined as $m^* k^2/\pi^2$,

where m^* is the mass ratio) and its bending stiffness (EI^*), thus dictates the foil's dynamics and the resulting aerodynamic performance [10]. Specifically, as f_b^* approximately falls in the range of 0.33 to 0.6, the foil can usually attain an optimal propulsive efficiency [10]. Hence, in this study f_b^* is selected as 0.45 when EI^* and m^* are moderate, i.e. $EI^* = 4$ and $m^* = 1$. Note that the above selected St and f_b^* values give rise to $k = \pi/2$ and $h_b^* = 0.6$, which are then fixed in all the cases. In addition, for simplicity, the ratio between the extra-driving-motion frequency and the base frequency, i.e., (f_e^*), is fixed at 2 throughout this study.

Equation 7 reveals that the dynamics of the flexible foil is affected by the competition among different types of forces, including the inertial force, tension force and bending force (the three terms on the LHS of Equations 7) as well as the fluid force (the term on the RHS of Equation 7). Since in this study the foil is assumed to be inextensible and its deformation is mainly caused by transverse forces, only the force competition along the transverse direction, involving the inertial force, bending force and fluid force, is considered. Generally, the inertial force and the fluid force result in torques about the foil's leading edge, hence promote or prevent the foil's deflection. However, the bending moment passively produced due to the foil's deflection always acts as a restoring torque, which prevents the foil from further deflection and forces the foil to return to its original shape. To describe such competitions, these competing forces/moments are evaluated as follows.

As will be explained in Section 2.3, in this study the base-motion frequency (f_b^*) is set as less than 1, which means that the foil's deformation is mainly determined by its first bending mode. Under this circumstance, the foil's transverse inertial force can be estimated from the y-component inertial forces at its leading and trailing edges, which are expressed as

$$F_{I,L,y}^* = -\frac{m^* k^2}{\pi^2} a_{L,y}^* \tag{11}$$

$$F_{I,T,y}^* = -\frac{m^* k^2}{\pi^2} a_{T,y}^* \tag{12}$$

where $a_{L,y}^*$ is the leading edge's y acceleration and can be derived from Equation 6

$$a_{L,y}^*(t^*) = -2h_b^*\pi^2\cos(2\pi t^*) - 2h_e^* f_e^{*2}\pi^2\cos(2\pi f_e^* t^* + \phi_e) \tag{13}$$

$a_{T,y}^*$ is the trailing edge's y acceleration, which is assessed during the simulation.

For the same reason, the bending moment usually achieves its maximum at the foil's leading edge, which can be expressed as

$$M_L^* = |EI^* \frac{\partial^2 \boldsymbol{X}^*}{\partial s^{*2}}(t^*, 0)| \tag{14}$$

Table 1: Definitions and selected values of dimensionless parameters in this study.

Dimensionless parameter	Definition	Values[2]
Bending stiffness	$EI^* = EI/\rho_f U_\infty^2 c^3$	0.8, 4, 16
Base-motion frequency[1]	$f_b^* = f_b/f_N = (2\pi/k_1^2)\sqrt{m^* k^2/\pi^2 EI^*}$	0.223, 0.447, 0.999
External force	$\boldsymbol{f}_E^* = \boldsymbol{f}_E c/U_\infty^2$	-
Fluid loading	$\boldsymbol{F}_f^* = \boldsymbol{F}_f/\rho_f U_\infty^2$	-
Frequency ratio	$f_e^* = f_e/f_b$	2
Base-motion amplitude	$h_b^* = h_b/c = St\pi/k$	0.6
Extra-driving-motion amplitude	$h_e^* = h_e/c$	0, 0.06, 0.15, 0.3, 0.45, 0.6
Reduced frequency	$k = \pi f_b c/U_\infty$	$\pi/2$
Mass ratio	$m^* = \rho_s/\rho_f c$	0.25, 1, 5
Pressure	$p^* = p/\rho_f U_\infty^2$	-
Reynolds number	$\mathrm{Re} = U_\infty c/\nu$	50, 200
Strouhal number	$St = f_b h_b/U_\infty$	0.3
Lagrangian coordinate	$s^* = s/c$	-
Time	$t^* = t f_b$	-
Tension force	$T^* = T/\rho_f U_\infty^2 c$	-
Velocity	$\boldsymbol{v}^* = \boldsymbol{v}/U_\infty$	-
Foil's position	$\boldsymbol{X}^* = \boldsymbol{X}/c$	-
Leading-edge y displacement	$y_L^* = y_L/c$	Prescribed by Equation 6
Extra-driving-motion phase angle	ϕ_e	0, $\pi/4$, $\pi/2$, ... , $7\pi/4$, $2\pi(0)$
Gradient operator	$\nabla^* = c\nabla$	-

[1] f_N is the first natural frequency of the flexible foil in vacuum, defined as $f_N = k_1^2\sqrt{EI/\rho_s}/2\pi c^2$, where $k_1 = 1.8751$ [24].

[2] symbol "-" indicates that the corresponding parameter is updated during the simulation.

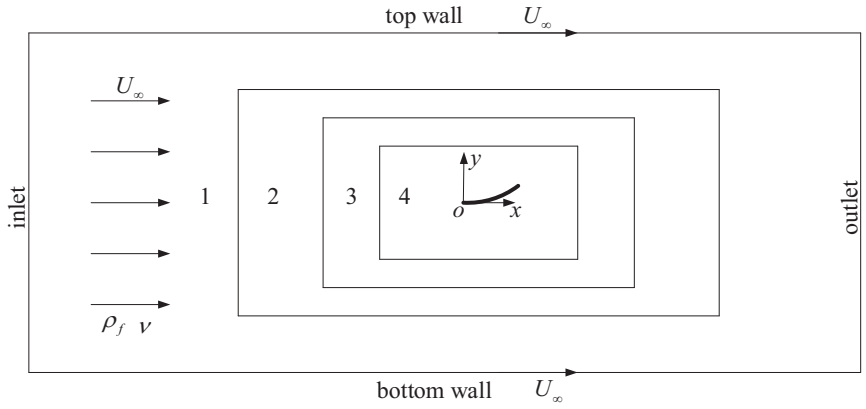

Figure 2: Computational domain with multi-block arrangement (not in scale).

In this study, M_L^* is defined as positive when the foil is upward-deflected, and negative if the other way around.

As for the fluid force, it can be evaluated through analyzing the distributed fluid loading along the foil, which will be presented during the discussion.

To evaluate the foil's aerodynamic performance and the associated power expenditure under various conditions, two coefficients, i.e., the thrust and power coefficients, are adopted and defined as

$$C_T = \frac{2F_T}{\rho_f U_\infty^2 c}$$
$$C_P = \frac{2P}{\rho_f U_\infty^3 c}$$

where F_T is the thrust and P is the input power defined as $P = F_{d,y}\dot{y}_L(t)$. $F_{d,y}$ is the vertical driving force applied at the foil's leading edge, and $\dot{y}_L(t)$ the leading edge's heaving velocity. Negative P or C_P indicates that energy is transferred from the foil to the driving system. Since this part of energy cannot be recovered, only positive P or C_P is taken into account when evaluating efficiencies in this study. Such a treatment was also adopted in Yin and Luo [12] and Shoele and Zhu [25]. Accordingly, the propulsive efficiency of the flexible foil can be calculated as

$$\eta = \frac{\bar{C}_T}{\bar{C}_{P_+}} \tag{15}$$

where $\bar{C}_T$ is the time-averaged thrust coefficient and $\bar{C}_{P_+}$ the time-averaged positive power coefficient.

2.2 Methodology

To facilitate this study, the incompressible D2Q9 MRT LBE model [26], i.e., two-dimensional incompressible multiple-relaxation-time lattice Boltzmann equation model with nine discrete velocities, is employed as an alternative numerical method for solving the two-dimensional Navier-Stokes equations. The MRT multi-block scheme proposed by Yu et al. [27] is applied to enhance the computational efficiency while maintaining sound accuracy. The finite difference method is adopted to solve Equations 7 and 8 for simulating the structure dynamics. The interplay between the fluid flow and the structure dynamics is linked using the immersed boundary method (IBM) [28], which is incorporated into the LBM for capturing moving boundaries and evaluating the fluid force on the foil. Details of the current numerical algorithm and its validation can be found in Appendix 4 and our previous work [29, 30, 31, 32].

Throughout this study, the computational domain is set as $60c$(L)×$40c$(W) with a uniform flow translating from the left to the right with a speed U_∞ = 0.01 (determined through the convergence test in Appendix 4), as shown in Figure 2. The flexible foil is placed $20c$ downstream from the inlet boundary, and the base heaving motion imposed at its leading edge is symmetric about the channel centerline. In addition, the entire computational domain is divided into four sets of blocks with the mesh density being increased by a factor of 2 as the block number increases. Around the foil, the block (Block 4) with the finest mesh spacing $\Delta x = c/96$ (also determined through the convergence test in Appendix 4) is used in the present study.

The boundary conditions are also specified in Figure 2. At the inlet, the non-reflecting inlet boundary condition proposed by Izquierdo and Fueyo [33] is used, whereas at the outlet, the homogenous Neumann boundary condition is implemented. The Dirichlet boundary condition is applied with the x velocity U_∞ and y velocity 0 on the top and bottom walls. On the foil's surface are imposed the no-slip and no-penetration boundary conditions.

2.3 Case summary

According to Section 2.1, the extra driving motion is described by three parameters, i.e., its frequency (f_e^*), amplitude (h_e^*) and phase angle (ϕ_e). In this study, the extra-driving-motion frequency is fixed at a value twice the base-motion frequency, i.e., $f_e^* = 2f_b^*$. Therefore, the foil's aerodynamic performance is mainly influenced by the change of the other two parameters. In addition, the performance can also be affected by the foil's bending stiffness (EI^*) and mass

Table 2: Key simulation results for the baseline case

Parameter	$\bar{C}_T$	η	$\bar{C}_{P_+}$	$\lvert D^* \rvert_{max}$
Value	0.43	0.101	4.27	0.21

ratio (m^*), and the fluid property represented by the Reynolds number (Re). Hence, this study is devoted to investigating the effects of extra driving motion with various amplitudes and phase angles on the aerodynamic performance of the foil with different bending stiffness and mass ratios heaving in the flow at selected Reynolds numbers. The values for these five parameters are chosen as follows. h_e^* varies from 0 to 0.6, covering six different values, where $h_e^* = 0$ means no extra driving motion, corresponding to the simple-driving-motion case. Eight ϕ_e values are chosen from 0 to 2π with an increment $\pi/4$. EI^* is set as 0.8, 4, 16 and m^* is selected as 0.25, 1 and 5. These EI^* and m^* values are close to those chosen by wide species of flying insects, such as fruit fly, bumble bee, dragonfly and hawkmoth [10, 34]. Under these circumstances, the base-motion frequency f_b^* is in the range of 0.223 to 0.999, indicating that the foil's deformation is mainly dictated by the first bending mode. Furthermore, the fluid-structure interaction problem is studied at two selected Reynolds numbers, i.e., Re = 50 and 200, which are slightly larger than the minimum Reynolds number (i.e., $O(10)$) adopted by natural flyers [1]. The selected values for these five parameters are also summarised in Table 1.

3 Results and Discussion

3.1 Effects of extra driving motion

Figure 3 gives an overview of the simulation results when the foil with moderate bending stiffness $EI^* = 4$ and mass ratio $m^* = 1$ undergoes the pure base heaving motion (denoted as the baseline case hereinafter) or the motion combining the base motion and extra driving motion with various amplitudes (h_e^*) and phase angles (ϕ_e) at Re = 200. For easy comparison, the data for the baseline case are represented by dashed horizontal lines, which are also listed in Table 2. Furthermore, according to Equation 6, one can get $y_L^*(t^*, \phi_e, h_e^*) = -y_L^*(t^* + 1/2, \phi_e + \pi, h_e^*)$, indicating that, for extra driving motion of a given amplitude, if its phase angle increases (or equivalently decreases) by π, the motion of the foil's leading edge is mirrored, and so is the foil's resulting dynamics. As such, only the results in the range of $0 < \phi_e < \pi$ are presented.

The first two rows of Figure 3 show the time-averaged thrust coefficient ($\bar{C}_T$) and propulsive

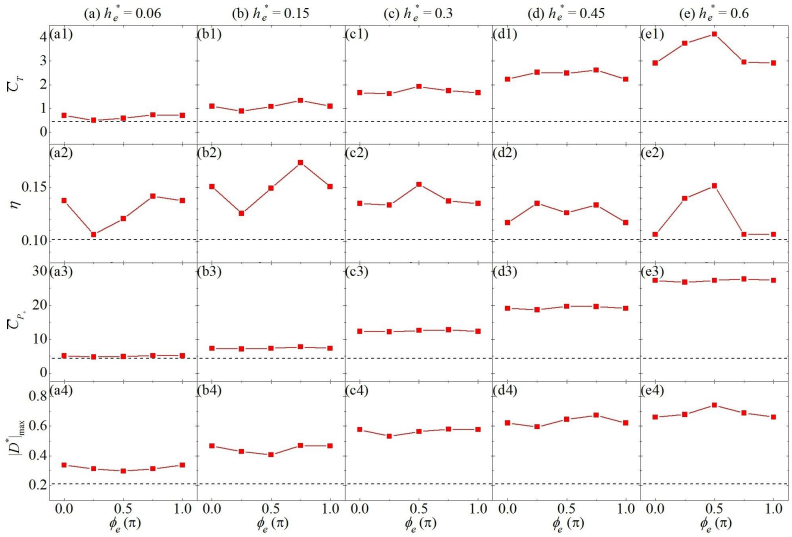

Figure 3: Variation of the foil's time-averaged thrust coefficient ($\bar{C}_T$), propulsive efficiency (η), time-averaged positive power coefficient ($\bar{C}_{P_+}$) and maximum absolute deflection ($|D^*|_{max}$) against the extra-driving-motion phase angle ϕ_e, under extra-driving-motion amplitude h_e^* = 0.06 (a), 0.15 (b), 0.3 (c), 0.45 (d) and 0.6 (e). The horizontal dashed lines represent the baseline case. The foil has the moderate bending stiffness and mass ratio, i.e., EI^* = 4 and m^* = 1, and heaves in a flow of Reynolds number Re = 200. All the values are evaluated based on the data collected over the $17th$ to $20th$ heaving cycles, within which the transient effect has disappeared.

efficiency (η), respectively, which represent the foil's propulsion performance. It is seen that the generated thrust $\bar{C}_T$ can be enhanced by any adopted extra driving motion. Such enhancement increases with the extra-driving-motion amplitude h_e^*. At given h_e^*, $\bar{C}_T$ approaches its maximum approximately at $\phi_e = \pi/2$ or $3\pi/4$, and its minimum at around $\phi_e = 0$ or $\pi/4$. The maximum $\bar{C}_T = 4.14$ among all the cases appears at $h_e^* = 0.6$ and $\phi_e = \pi/2$, which is about ten times of the value $\bar{C}_T = 0.43$ in the baseline case.

The efficiency η is also improved, as shown in the second row of Figure 3. At given h_e^*, its variations against ϕ_e are similar to the corresponding $\bar{C}_T$ curves. But it does not vary too much with h_e^*. Its maximum $\eta = 0.173$ among all the cases appears at $h_e^* = 0.15$ and $\phi_e = 3\pi/4$, improved by about 70% if compared with the value $\eta = 0.101$ in the baseline case. Compared with the improvement in thrust, however, this improvement is much less significant. This is because that the introduction of extra driving motion also consumes a significant amount of additional driving power, which increases with h_e^*, as revealed in the third row of Figure 3.

The last row of Figure 3 reveals that the foil's maximum deflection $|D^*|_{max}$ (defined as $|D^*|_{max} = \max(|y_T^* - y_L^*|)$, where y_L^* and y_T^* are the leading- and trailing-edge y displacements, respectively) is enhanced by the extra driving motion. Furthermore, similar to the variation in $\bar{C}_T$, its increment also increases with h_e^* regardless of the extra-driving-motion phase angle. This suggests that $|D^*|_{max}$, $\bar{C}_T$ and h_e^* are positively correlated, consistent with the finding by Kang et al. [10] that $|D^*|_{max}$ and $\bar{C}_T$ is positively correlated for flapping foils.

To unveil the reason for the improvement in the thrust, two representative cases are selected for detailed investigation, i.e., the baseline case and the case with $\phi_e = 3\pi/4$ and $h_e^* = 0.15$, the latter attaining the most significant thrust improvement in its h_e^* group. In these two cases, the data collected from the 21st heaving cycle are used for discussion, and the instant at the beginning of this cycle is defined as $t^* = 0$ for convenience.

In the baseline case, since only a purely sinusoidal motion is imposed at the foil's leading edge, the foil's deformation process in the upstroke is mirrored from that in the downstroke, as evidenced by the time histories of the leading- and trailing-edge y displacements shown in Figures 4(a) and 4(b), respectively. Hence, only the dynamics in the downstroke (shaded region in Figure 4) is discussed.

It is seen from Figure 4 that, due to the foil's flexility, the trailing-edge y displacement lags a bit (about 0.06 in time) behind the leading-edge y displacement, but with a significantly larger amplitude. Given that for sinusoidal motions acceleration is antiphase with displacement and

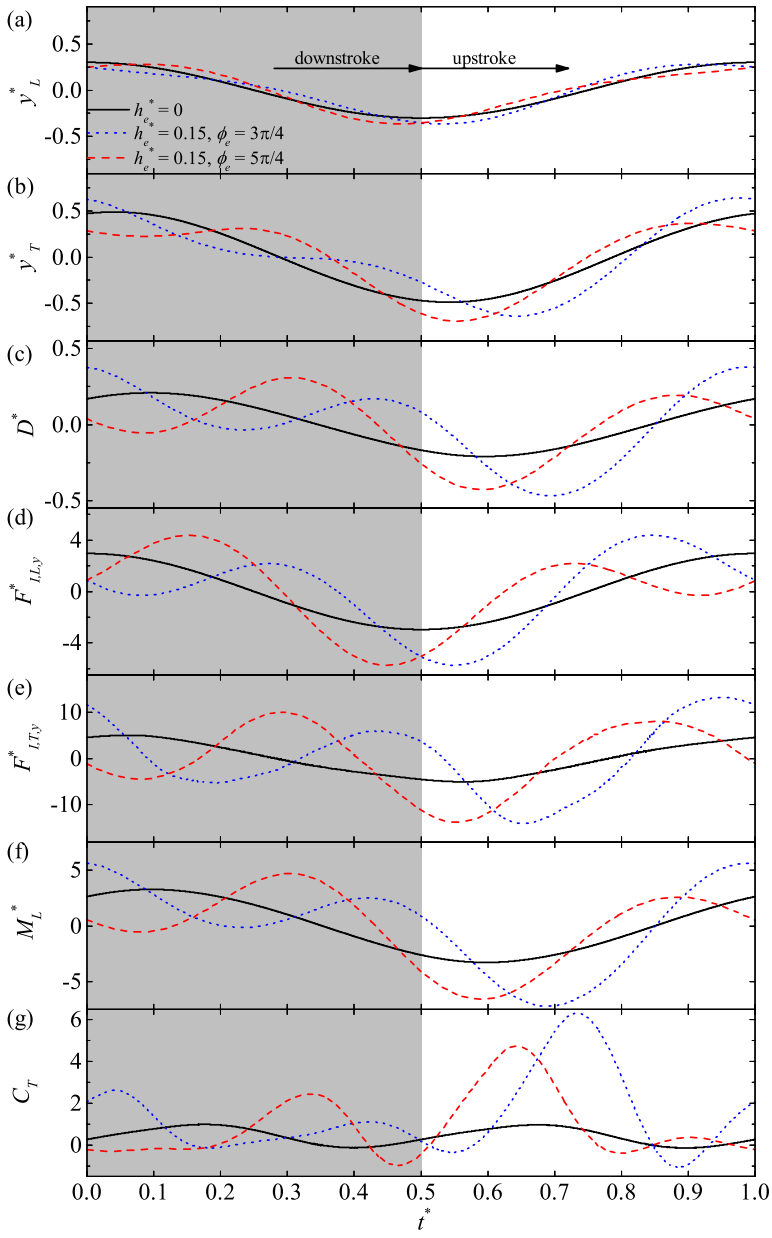

Figure 4: Time histories of the (a) leading-edge y displacement (y_L^*), (b) trailing-edge y displacement (y_T^*), (c) deflection (D^*), (d) leading-edge y inertial force ($F_{I,L,y}^*$), (e) trailing-edge y inertial force ($F_{I,T,y}^*$), (f) bending moment at the leading edge (M_L^*), and (g) thrust coefficient (C_T) for the baseline case where $h_e^* = 0$, the case with $h_e^* = 0.15$ and $\phi_e = 3\pi/4$, and the case with $h_e^* = 0.15$ and $\phi_e = 5\pi/4$, when $EI^* = 4$ and $m^* = 1$.

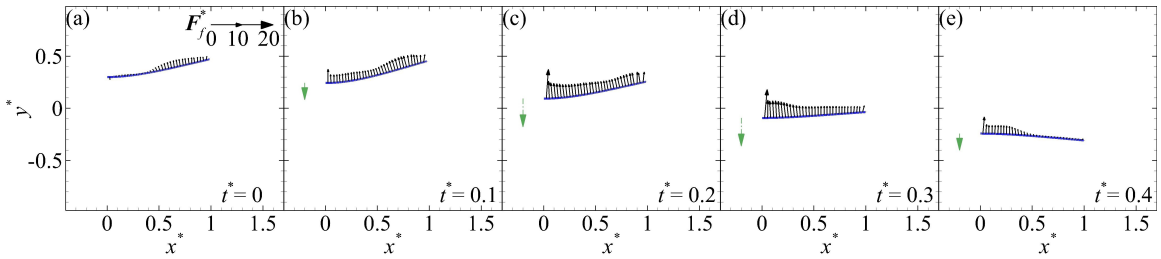

Figure 5: Distribution of dimensionless fluid loading ($\boldsymbol{F}_f^*$) over the heaving flexible foil during the downstroke in the baseline case. The dashed triangle-headed arrow indicates the foil's heaving direction, and its length reflects the heaving speed.

also antiphase with inertial force as described in Equations 11 and 12, the leading- and trailing-edge y inertial forces ($F_{I,L,y}^*$ and $F_{I,T,y}^*$) are in phase with their respective displacements, as evidenced in Figure 4. It is also observed from Figures 4(c) and 4(f) that the bending moment at the leading edge M_L^* follows the trend of the foil's deflection D^*, indicating a positive correlation between these two quantities. Furthermore, the thrust C_T repeats twice within one heaving cycle with its peaks appearing slightly after the peak/though of the bending moment (about 0.07 in time).

The evolution of various parameters shown in Figure 4 together with the fluid loading ($\boldsymbol{F}_f^*$) along the foil at selected instants shown in Figure 5 reflect the consequence of force competition on the foil's dynamics. Specifically, during the first half of the downstroke, i.e., $t^* < 0.25$, the inertial force along the foil is generally oriented upwards as indicated by the positive leading- and trailing-edge y inertial forces shown in Figures 4(d) and 4(e), and the fluid loading points roughly along the same direction, as shown in Figures 5(a) to 5(c). Thus, the inertial force and the fluid force collaborate to further the foil's upward deflection during this period. Therefore, the bending moment at the leading edge M_L^* remains positive, as shown in Figure 4(f), trying to recover the foil's shape from its upward deformation.

At $t^* = 0.1$, the foil achieves its largest upward deflection, as shown in Figure 4(c). At this instant, the bending moment approaches its maximum $M_L^* = 3.28$. The foil then starts to recover its shape, during which its underneath fluid is repelled downward and downstream. Accordingly, the upward- and upstream-oriented fluid loading acts on the foil as the reaction force, as evidenced by Figure 5(b). This fluid loading slightly increases as the upward-oriented inertial force reduces with time, leading to the maximum instantaneous thrust $C_T = 0.99$ at around $t^* = 0.17$, as shown in Figure 4(g). This explains the slight time delay of the maximum thrust behind the maximum bending moment as revealed in Figure 4.

During the second half of the downstroke, i.e., $0.25 < t^* < 0.5$, the foil first recovers its original shape at the beginning, and then starts to deflect downward under the reversed inertial force, as evidenced at the two instants shown in Figures 5(d) and 5(e). During this period, the fluid loading still points upwards, which then generates drag when the foil deflects downward, as confirmed in Figure 4(g). Compared to the thrust produced in the first half of the downstroke, however, this drag is relatively smaller. Hence a net thrust is obtained in this baseline case.

In the case with $\phi_e = 3\pi/4$ and $h_e^* = 0.15$, the foil's leading-edge y displacement does not vary purely sinusoidally, as shown in Figure 4(a). Thus, unlike in the baseline case, in this case the foil's deformation processes during the downstroke and during the upstroke are not mirrored, and C_T does not repeat twice within one heaving cycle, as shown in Figure 4. It is noticed that the leading-edge y displacement only deviates a little from that in the baseline case. This slight deviation, however, leads to significant changes to other parameters, implying that introducing small extra driving motion into the base motion can result in substantial changes to the foil's dynamics and aerodynamic performance. This can be attributed to that the extra-driving-motion frequency f_e is twice the base-motion frequency f_b. For the extra-driving-motion amplitude $h_e^* = 0.15$, the amplitude of the leading-edge y inertial force at the extra-driving-motion frequency then becomes the same as that at the base-motion frequency, as indicated by Equations 11 and 13. As such, the instantaneous leading-edge y inertial force is greatly increased at around $t^* = 0.55$ and 0.85 in this case, as shown in Figure 4(d).

At $t^* = 0.55$, the leading-edge y inertial force approaches its downward maximum, i.e., $F_{I,L,y}^* = -5.74$, about twice of that in the baseline case. This causes the successive increase in the inertial force along the foil as it moves upwards. At $t^* = 0.65$, the trailing-edge y inertial force approaches its downward maximum $F_{I,T,y}^* = -14.02$, about three times of that in the baseline case. Hence, the downward-oriented inertial force acting on the whole foil during this period is much larger than that in the baseline case. Furthermore, the fluid loading is also oriented along the same direction during this period, whose strength is generally larger than in the baseline case, as indicated by Figures 6(b) and 6(c) and the mirrored images of Figures 5(b) and 5(c). As such, these two types of forces collaboratively result in a much larger deflection that is accompanied by a much larger bending moment.

At $t^* = 0.69$, the leading-edge bending moment approaches its negative maximum, i.e., $M_L^* = -7.22$, more than twice of that in the baseline case. This greatly enhanced bending moment forces the foil to revert much faster. This can be evidenced by the fact that the foil

deflection changes from its negative maximum ($D^* = -0.47$ at $t^* = 0.69$) to its positive maximum ($D^* = 0.38$ at $t^* = 0.99$) within just 0.3 heaving cycle, whereas the foil spends much more time, i.e., a half heaving cycle, undergoing the same process with deflections of much less magnitudes in the baseline case, as shown in Figure 4(c). Hence, the foil accelerates its upper-side fluid upwards and downstream more rapidly, attaining much larger fluid loading at $t^* = 0.7$, as revealed by comparing Figure 6(c) and the mirrored image of Figure 5(c). Furthermore, the initial deflection of this rapid heaving process, i.e., $D^* = -0.47$ at $t^* = 0.69$, is more than twice of that at $t^* = 0.59$ in the baseline case, as shown in Figure 4(c). This larger downward deflection enables the foil to experience more upstream-oriented components of the fluid loading, hence further enhances the thrust. As a result of these two factors, the thrust reaches its maximum $C_T = 6.31$ at $t^* = 0.73$ (see Figure 4(g)), more than six times of that in the baseline case.

Likewise, the augmented leading-edge y inertial force at around $t^* = 0.85$ is able to induce a larger deflection with a larger bending moment. As such, the fluid loading is augmented and also more oriented towards upstream at around $t^* = 1$ (or at around $t^* = 0$ due to the periodicity) than in the baseline case, as shown in Figures 5(a) and 6(a). Eventually, the thrust is also notably increased at around $t^* = 1.04$ (or $t^* = 0.04$).

The above discussions reveal that the thrust generation depends on two major factors. One is the foil's deflection D^* determining the orientation of fluid loading, and the other is the foil's shape recovering rate reflecting the magnitude of fluid loading. If both or at least one of these two factors is improved, the thrust is very likely enhanced. Also, despite some delay, it is found that the foil's deflection D^* evolves in a similar way as the leading-edge y inertial force $F^*_{I,L,y}$, since the foil experiences the fundamental bending-mode vibration due to the fact that both the base-motion and extra-driving-motion frequencies are smaller than the foil's first natural frequency, i.e., $f_b < f_N$ and $f_e < f_N$. Therefore, *the generated thrust can be qualitatively estimated from the $F^*_{I,L,y}$ maxima and their following rate of change.*

The above criterion is found to be valid for all the cases illustrated in Figure 3. On one hand, with the increase of extra-driving-motion amplitude, generally the leading-edge y inertial force $F^*_{I,L,y}$ and its rate of change become larger, thus the thrust increases. On the other hand, the change of extra-driving-motion phase angle h^*_e also affects $F^*_{I,L,y}$ and its rate of change, and hence the generated thrust. For example, at a given $h^*_e = 0.15$, the case with $\phi_e = 5\pi/4$ achieves its global maximum $F^*_{I,L,y}$ (in negative sign) at $t^* = 0.45$ and hence its maximum thrust with some delay at around $t^* = 0.64$, as revealed in Figures 4(d) and 4(g). If compared with the case with $\phi_e = 3\pi/4$, even though the negative $F^*_{I,L,y}$ maxima are identical in these two cases (Note

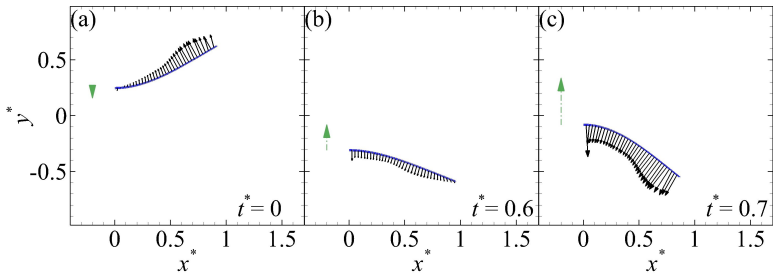

Figure 6: Distribution of dimensionless fluid loading ($\boldsymbol{F}_f^*$) over the heaving flexible foil at selected instants, in the case with $EI^* = 4$, $m^* = 1$, $h_e^* = 0.15$ and $\phi_e = 3\pi/4$. The dashed triangle-headed arrow indicates the foil's heaving direction, and its length reflects the heaving speed.

that the $F_{I,L,y}^*$ evolution in these two cases are mirrored from each other about $t^* = 0$ or 0.5, as shown in 4(d)), the following rate of change in the case with $\phi_e = 5\pi/4$ is smaller. Consequently, its peak thrust is smaller, as clearly shown in Figure 4(g). Furthermore, a detailed comparison among all the cases in this h_e^* group unveils that either the global maximum $F_{I,L,y}^*$ or its following rate of change becomes smaller when ϕ_e deviates from $3\pi/4$. As a result, the peak thrust and accordingly the time-averaged thrust are smaller than those in the case with $\phi_e = 3\pi/4$.

Although not presented here for brevity, it is found that when $f_e^* = 1$ and 1.5, i.e., the extra-driving-motion frequency is set as around 0.45 and 0.67 times of the foil's first natural frequency, and by keeping the amplitude of extra-driving-motion induced leading-edge y inertial force unchanged, similar or even better improvements in the foil's deflection and net thrust can be achieved as compared to in the cases with $f_e^* = 2$ (i.e., 0.89 times of the foil's first natural frequency). This indicates that the extra-driving-motion frequency being close to the foil's first natural frequency does not play a determining role in enhancing the foil's propulsion performance.

3.2 Effects of bending stiffness

The previous section explains why and how the foil's thrust is enhanced by means of extra driving motion, for the cases with the moderate bending stiffness $EI^* = 4$ and mass ratio $m^* = 1$. Equations 11, 12 and 14 also clearly show that the bending stiffness and mass ratio can affect the inertial force and bending moment, thus their competition, and ultimately the foil's dynamics and aerodynamic performance. Nevertheless, whether similar improvements can be achieved if the foil becomes more flexible/stiffer or lighter/heavier remains unknown. To

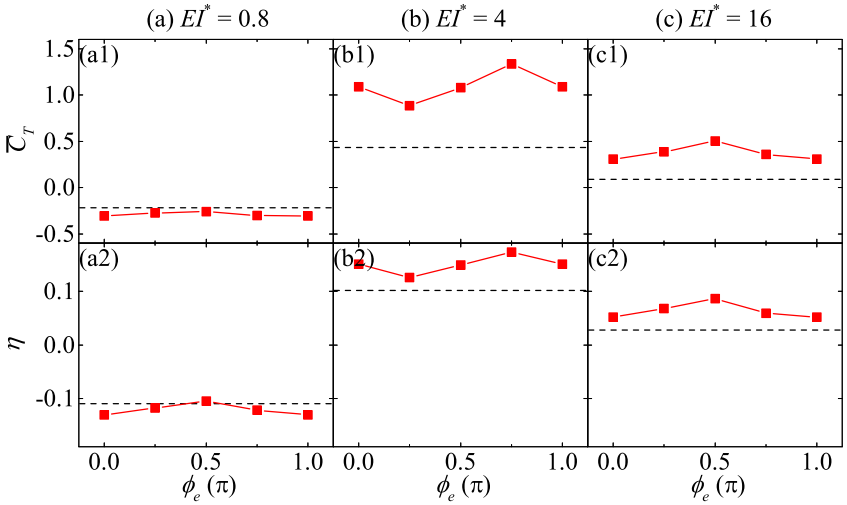

Figure 7: Variation of time-averaged thrust coefficient ($\bar{C}_T$) and propulsive efficiency (η) against extra-driving-motion phase angle ϕ_e for the foil with the moderate mass ratio m^* = 1 and bending stiffness EI^* = 0.8 (a), 4 (b) and 16 (c) heaving with extra driving motion of amplitude h_e^* = 0.15. The horizontal dashed lines represent the simple-driving-motion cases.

address this issue, investigations on the effects of the foil's bending stiffness and mass ratio are performed in this and next sections.

Figure 7 shows the time-averaged thrust coefficient ($\bar{C}_T$) and propulsive efficiency (η) for the cases where the foil with the bending stiffness EI^* = 0.8, 4 and 16 and moderate mass ratio m^* = 1 heaves with the pure base motion and with the complex driving motions with extra-driving-motion amplitude h_e^* = 0.15 and phase angle ϕ_e varying from 0 to π. Note that the cases with EI^* = 4 have been discussed in Section 3.1, and Figure 7(b) is directly reproduced from Figures 3(b1) and 3(b2) for ease of comparison.

When the foil becomes more flexible with EI^* = 0.8, both the thrust $\bar{C}_T$ and efficiency η are negative in the simple-driving-motion case, as shown in Figure 7(a), meaning that a drag instead of a thrust is produced. This degradation in the propulsion performance originates from the fact that, as the foil becomes more flexible, the bending moment plays a much less role in the foil's dynamics, and hence the foil's dynamics is dominated by the other two types of forces, i.e., the fluid force and the inertial force. Under this condition, the fluid and inertial forces are generally a pair of action and reaction forces, as described in Equations 7, 11 and 12. Such a relation can also be evidenced by examining these two forces at a selected instant t^* = 0.1, as shown in Figures 8(b) and 9(a). At this instant, the leading- and trailing-edge y inertial forces ($F^*_{I,L,y}$ and $F^*_{I,T,y}$) are positive, i.e., upward-oriented, as revealed in Figures 8(c) and 8(d), but the fluid loading mainly points downwards (see Figure 9(a)). Since the fluid

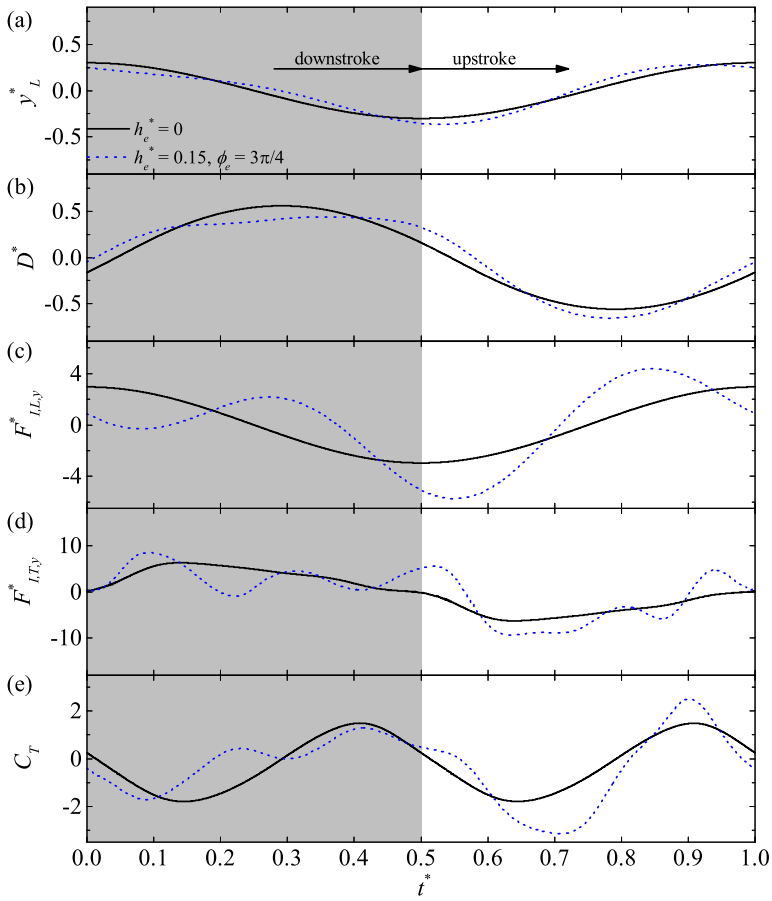

Figure 8: Time histories of the (a) leading-edge y displacement (y_L^*), (b) deflection (D^*), (c) leading-edge y inertial force ($F_{I,L,y}^*$), (d) trailing-edge y inertial force ($F_{I,T,y}^*$), and (e) thrust coefficient (C_T) in the simple-driving-motion case where $h_e^* = 0$ and the case with $h_e^* = 0.15$ and $\phi_e = 3\pi/4$, when $EI^* = 0.8$ and $m^* = 1$.

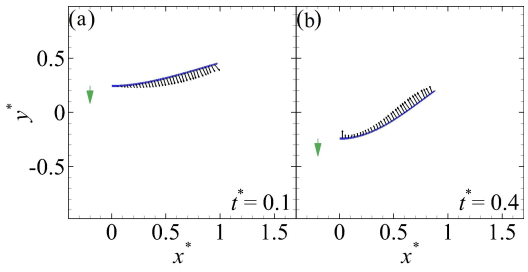

Figure 9: Distribution of dimensionless fluid loading ($\boldsymbol{F}_f^*$) over the heaving flexible foil at selected instants in the simple-driving-motion case with $EI^* = 0.8$ and $m^* = 1$. The dashed triangle-headed arrow indicates the foil's heaving direction, and its length reflects the heaving speed.

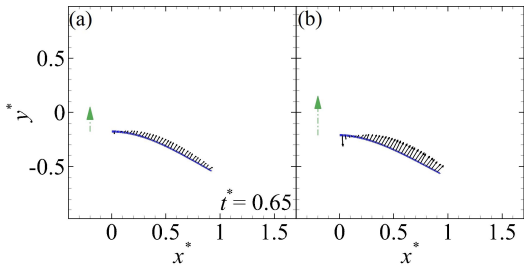

Figure 10: Distribution of dimensionless fluid loading ($\boldsymbol{F}_f^*$) over the heaving flexible foil in the simple-driving-motion case with EI^* = 0.8 and m^* = 1 (a) and the case with h_e^* = 0.15 and ϕ_e = $3\pi/4$ (b) at t^* = 0.65. The dashed triangle-headed arrow indicates the foil's heaving direction, and its length reflects the heaving speed.

loading also points slightly downstream due to the foil's upward deflection, it produces drag to the foil, as confirmed in Figures 8. This is quite different from that in the simple-driving-motion case with moderate flexibility EI^* = 4 (i.e., the baseline case), where thrust is produced mainly in the first half of each stroke (See Figure 4(g)). In the current case the much smaller bending moment cannot effectively support the shape recovering process and hence induce thrust. Even though thrust can be produced as the foil reverts in the second half of each stroke, say at around t^* = 0.4 as shown in Figure 9(b), it is induced by the inertial force and not strong enough to compensate the drag produced in the first half stroke, as revealed in Figure 8(e). Therefore, the net thrust is slightly negative in this simple-driving-motion case.

When the extra driving motion is introduced, no improvement is observed, unlike in the cases with EI^* = 4. On the contrary, it is even worse regardless of the extra-driving-motion phase angle ϕ_e, as revealed in Figure 7(a). Although unexpected, this degradation is because that the inertial force enhanced by the extra driving motion can induce extra anti-phase, downstream-oriented fluid force, and hence extra drag. This can be confirmed by comparing the forces produced in one representative case, i.e., the case with ϕ_e = $3\pi/4$, with those in the simple-driving-motion case. For example, at around t^* = 0.65, the inertial force points downwards in both cases, but it is larger in the complex-driving-motion case, as revealed in Figures 8(c) and 8(d). Since the fluid force is roughly equal and opposite to the inertial force, the fluid loading is upward- and downstream-oriented in both cases, but larger in the complex-driving-motion case, as shown in Figure 10. Therefore, the drag increases around this instant in the complex-driving-motion case, as confirmed in Figure 8(e).

Note that the criterion introduced in Section 3.1, i.e., the generated thrust can be qualitatively estimated from the $F_{I,L,y}^*$ maxima and their following rate of change, is no longer valid in

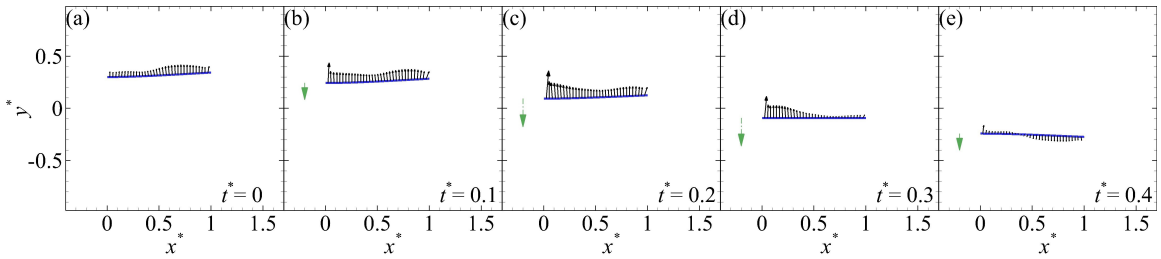

Figure 11: Distribution of dimensionless fluid loading ($\boldsymbol{F}_f^*$) over the heaving flexible foil during the downstroke in the simple-driving-motion case with $EI^* = 16$ and $m^* = 1$. The dashed triangle-headed arrow indicates the foil's heaving direction, and its length reflects the heaving speed.

this complex-driving-motion case. The reason is because in this case the applied extra-driving-motion frequency, f_e, is about twice of the foil's first natural frequency, f_N, and hence the foil experiences high-order oscillations, as reflected by the irregular D^* and $F^*_{I,T,y}$ fluctuations shown in Figures 8(b) and 8(d).

When the foil becomes much stiffer with $EI^* = 16$, positive thrust $\bar{C}_T = 0.09$ and efficiency $\eta = 0.028$ can be attained in the simple-driving-motion case, and both of them can be improved by introducing the extra driving motion regardless of the phase angle ϕ_e, as shown in Figure 7(c). At $\phi_e = \pi/2$, $\bar{C}_T$ and η approach their respective maxima $\bar{C}_T = 0.5$ and $\eta = 0.086$, more than five and three times of the values in the simple-driving-motion case, respectively. A close inspection reveals that the mechanisms for thrust generation in the simple-driving-motion case and extra-driving-motion-induced thrust enhancement are the same as those in the cases with moderate flexibility $EI^* = 4$. Hence, they are not repeated here for the sake of brevity. Despite of these similarities, it is observed from Figures 7 that the stiffer foil produces significantly smaller thrust than the foil with $EI^* = 4$ under the same leading-edge forcing condition. This is because that the stiffer foil requires less deformation to balance a similar amount of inertial and fluid forces. Thus, the interaction of the fluid with the heaving foil mainly occurs in the vertical direction, as evidenced by the fluid loading distribution over the foil during the downstroke in the simple-driving-motion case shown in Figure 11. As a result, less horizontal force, or thrust, is generated.

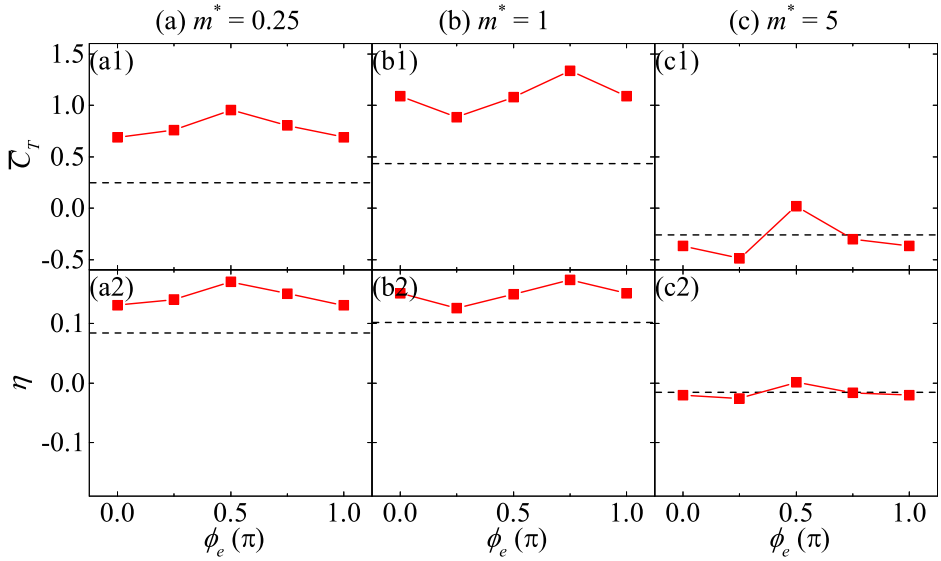

Figure 12: Variation of time-averaged thrust coefficient ($\bar{C}_T$) and propulsive efficiency (η) against extra-driving-motion phase angle ϕ_e for the foil with the moderate bending stiffness EI^* = 4 and the mass ratio m^* = 0.25 (a), 1 (b) and 5 (c) heaving with extra driving motion of amplitude h_e^* = 0.15. The horizontal dashed lines represent the simple-driving-motion cases.

3.3 Effects of mass ratio

Figure 12 shows the time-averaged thrust coefficient ($\bar{C}_T$) and the propulsive efficiency (η) for the cases where the foil with moderate bending stiffness EI^* = 4 and mass ratio m^* = 0.25, 1 and 5 heaves with the pure base motion and with the complex driving motions of extra-driving-motion amplitude h_e^* = 0.15 and phase angle ϕ_e varying from 0 to π.

When the foil becomes lighter with m^* = 0.25, positive thrust $\bar{C}_T$ = 0.25 and efficiency η = 0.084 are produced in the simple-driving-motion case, and they can be improved by the extra driving motion with any ϕ_e, just like in the cases with m^* = 1 as discussed in Section 3.1. However, when m^* = 0.25 the thrust in both the simple-driving-motion and complex-driving-motion cases is generally smaller than that when m^* = 1, as revealed in Figures 12(a1) and 12(b1). This can be attributed to the fact that when the foil is lighter, less inertial force is induced, resulting in smaller deformation and hence smaller thrust.

It is interesting to see that, when comparing Figure 12(a) with Figure 7(c), the propulsion performance in the cases with EI^* = 4 and m^* = 0.25 and in the cases with EI^* = 16 and m^* = 1 is qualitatively alike. This similarity stems from the fact that these two cases share an identical ratio of EI^* to m^*, i.e., EI^*/m^* = 16. Hence, the competitions between the bending moment and the inertial force in these two sets of cases are similar as indicated in Equations

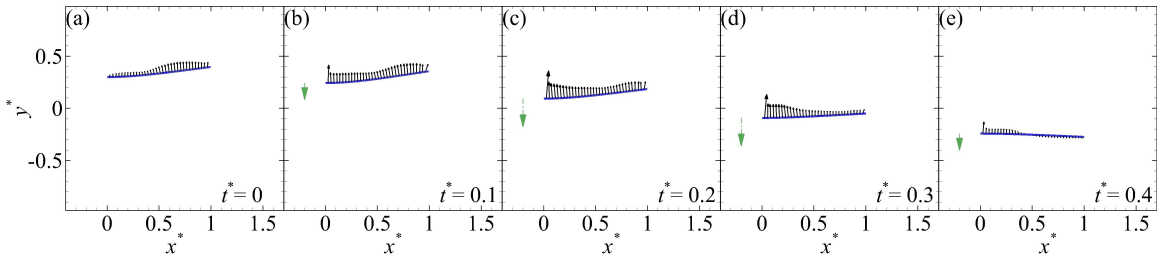

Figure 13: Distribution of dimensionless fluid loading ($\boldsymbol{F}_f^*$) over the heaving foil during the downstroke for the simple-driving-motion case with $EI^* = 4$ and $m^* = 0.25$. The dashed triangle-headed arrow indicates the foil's heaving direction, and its length reflects the heaving speed.

7 and 14, which leads to similar aerodynamic performance for the foil. The similar force competitions can also be evidenced by the foil's deformation and fluid loading distribution during the downstroke in the two simple-driving-motion cases, as shown in Figures 11 and 13. Furthermore, this similarity also confirms the key role of the dimensionless base-motion frequency ($f_b^* = 2\pi/k_1^2\sqrt{m^*k^2/\pi^2 EI^*}$), where the EI^* to m^* ratio appears, in determining the foil's dynamics and aerodynamic performance [10].

Likewise, for the cases with $m^* = 5$, since their EI^* to m^* ratio is 0.8, identical to that in the cases with $m^* = 1$ and $EI^* = 0.8$ which have been discussed in Section 3.2, the foil fails to produce effective thrust in the simple-driving-motion case, and no obvious improvement is obtained through the extra driving motion, either, as revealed in Figure 12(c).

3.4 Effects of Reynolds number

Besides the bending stiffness and the mass ratio, the Reynolds number Re also affects the heaving foil's dynamics and aerodynamic performance. It describes the fluid's inertia-to-viscosity ratio, thus determines the fluid loading acting on the foil. To examine the influence of Reynolds number on the heaving foil's aerodynamic performance and also on the effectiveness of extra driving motion, a series of additional cases with Re = 50 and the other parameters remaining identical to those in the cases explored in Section 3.1 is simulated. All the simulated time-averaged thrust coefficient ($\bar{C}_T$) and propulsive efficiency (η) are plotted in Figure 14. Since as revealed in Section 3.1 the foil's maximum deflection ($|D^*|_{max}$) is positively correlated with the extra-driving-motion amplitude, all the data are plotted against $|D^*|_{max}$, similar to the way adopted in Kang et al. [10].

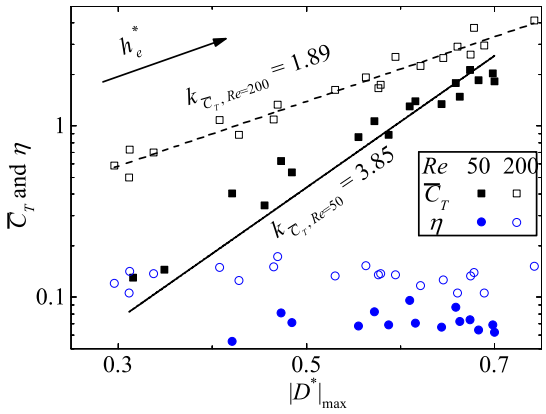

Figure 14: Variation of time-averaged thrust coefficient ($\bar{C}_T$) and propulsive efficiency (η) against the maximum absolute deflection ($|D^*|_{max}$) for the foil undergoing complex-driving-motion motions with extra-driving-motion amplitude (h_e^*) varying from 0.06 to 0.6 and phase angle (ϕ_e) varying from 0 to π, in the flows of Reynolds number Re = 50 and 200. The foil has the moderate bending stiffness and mass ratio, i.e., $EI^* = 4$ and $m^* = 1$. Note that, at Re = 50, the simple-driving-motion case reads $\bar{C}_T = -0.06$, $\eta = -1.4\%$ and $|D^*|_{max} = 0.22$, and at Re =200, the simple-driving-motion case reads $\bar{C}_T = 0.43$, $\eta = 10.1\%$ and $|D^*|_{max} = 0.21$.

It is seen from Figure 14 that, with the increase of Reynolds number, both the thrust and propulsive efficiency are enhanced. This is not surprising because, as Re increases, the viscosity plays a less role in the fluid-foil interaction, resulting in a reduction of the drag component of the fluid loading, and hence the enhancement of the thrust and efficiency. It is also confirmed from Figure 14 that, with the introduction of extra driving motion, the thrust can be improved (Note that the thrust is $\bar{C}_T = -0.06$ and 0.43 at Re = 50 and 200, respectively, in the simple-driving-motion cases), and the improvement increases with the maximum deflection $|D^*|_{max}$ or the extra-driving-motion amplitude h_e^*. This, again, confirms the positive correlations among $\bar{C}_T$, $|D^*|_{max}$ and h_e^*. Interestingly, the current results reveal that the increase of Reynolds number causes the reduction in the increasing rate of the thrust. As depicted in Figure 14, at Re = 200 the power of the increase in thrust is $k_{\bar{C}_T,\mathrm{Re=200}} = 1.89$, which is only a half of that at Re = 50, i.e., $k_{\bar{C}_T,\mathrm{Re=50}} = 3.85$. As for the propulsive efficiency, it seems less dependent of the maximum deflection or the extra-driving-motion amplitude, indicating that the generation of a larger thrust usually requires more power input regardless of the Reynolds number.

4 Conclusion

We numerically studied the influence of complex driving motion on the dynamics and resulting propulsion performance of a flexible foil heaving in the flight regimes of natural flyers. Extra driving motion of different amplitudes (h_e^*) and phase angles (ϕ_e) is imposed on the leading edge of the foil that has already undergone a harmonic base motion. The major findings are as follows:

1. When the foil's bending stiffness and mass ratio are moderate, i.e., $EI^* = 4$ and $m^* = 1$, both the inertial force and the bending force of comparable strength participate in the force competition, and hence large thrust can be generated. The extra driving motion can greatly enhance both the thrust and propulsive efficiency. The improvement in thrust increases with h_e^*. At a given h_e^*, there exists an optimal ϕ_e. As for the propulsive efficiency, since the introduction of extra driving motion requires additional power input, it is not as much improved as the thrust, and does not vary too much with h_e^*.

2. As the foil becomes much stiffer or lighter, i.e., EI^*/m^* significantly increases, the bending force plays a dominant role in the force competition. As such, the foil's deformation becomes smaller, leading to the generation of less thrust. In this case, the influence of extra driving motion is similar to that for the foil with moderate properties.

3. As the foil becomes much more flexible or heavier, i.e., EI^*/m^* significantly reduces, the inertial force plays a dominant role in the force competition. The fluid force required to balance the inertial force is oriented downstream during the first half of each stroke, hence generates drag instead of thrust. The extra driving motion makes the situation even worse.

4. If both the base-motion and extra-driving-motion frequencies are smaller than the foil's first natural frequency, the change in generated thrust can be qualitatively estimated by the change of two prescribed quantities: the maximum absolute value of the leading-edge y inertial force $F_{I,L,y}^*$ and its following rate of change. If both or at least one of them is improved, e.g., by the extra driving motion, the thrust is very likely enhanced. This criterion is found to be valid for all the eligible cases in this study.

5. Although the extra driving motion can improve the heaving foil's propulsion performance in flows of different Reynolds numbers, the thrust's increasing rate with respect to the

foil's maximum deflection $|D^*|_{max}$ (or equivalently the extra-driving-motion amplitude h_e^*) reduces with the Reynolds number.

This study confirms that the propulsion performance of a flexible heaving foil can be enhanced by incorporating extra driving motion into a purely harmonic motion. This, to some extent, explains why natural flyers do not adopt purely harmonic flapping motions [18, 19], and why more realistic kinematics should be taken into account in flapping-wing studies. Although inspiring, it should be pointed out that the three-dimensional effect which is an important factor for the natural flyers is not considered in this study. Furthermore, the effects of several other important parameters, such as the Strouhal number, the reduced frequency and the frequency ratio, are not explored when the extra driving motion is incorporated. All of these will be systematically investigated in our near-future work.

Appendix

A.1 Validation

To validate the current fluid-structure interaction numerical framework, three cases are selected and simulated for different validation purposes. The first case is for validating the pure solid structure solver, the second is for the pure fluid solver, and the third is for the fluid-structure coupling solver. For each case, the results obtained from the present numerical framework are compared with the analytical or numerical results from the literature.

In the first case, a filament is initially pinned at one of its ends with a position angle ($\Theta_0 = \pi/100$) relative to its equilibrium location. After released from the rest in vacuum, the filament keeps swinging under the influence of the gravity. If the bending stiffness of the filament can be negligible, the lateral displacement of any point on the filament at anytime can be evaluated by [23]

$$y(t,s) = \sum_{i=1}^{\infty} \frac{4\Theta_0 l}{z_i^2} \frac{J_2(z_i)}{J_1^2(z_i)} J_0\left(z_i\sqrt{\frac{s}{l}}\right) \cos\left(\frac{z_i t}{2}\sqrt{\frac{g}{l}}\right) \tag{16}$$

where l is the filament length, s the arc-length along the filament measured from its free end, g the gravitational acceleration, J_1 and J_2 the first and second bessel functions, and z_i the ith real root of the equation $J_0(z) = 0$. Through summing up the first 20 terms in Equation 16, the analytic solution of the time-dependent non-dimensional lateral displacement of the

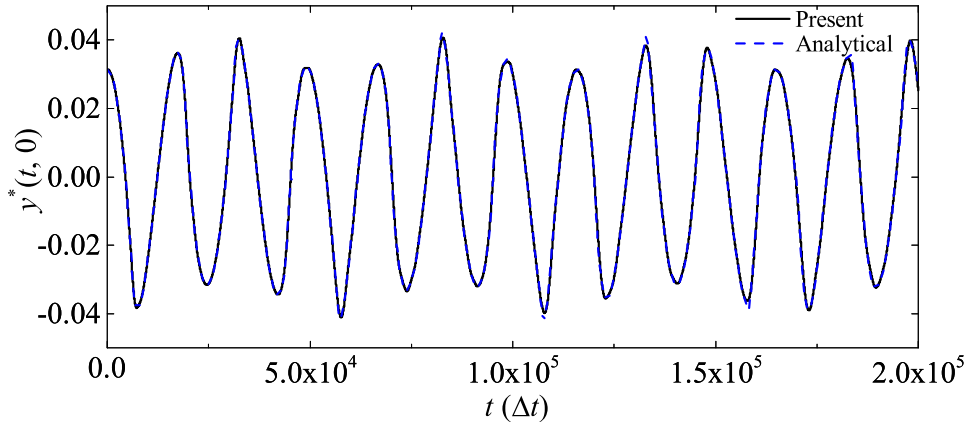

Figure 15: Time histories of the filament's free-end displacement.

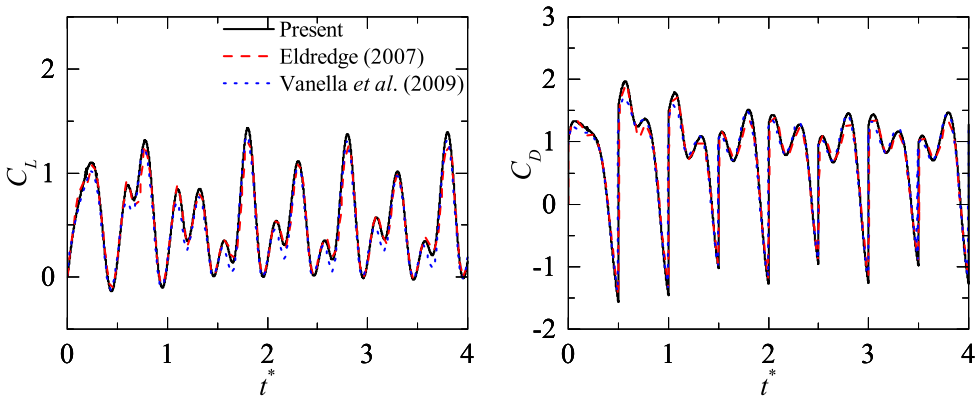

Figure 16: Time histories of the lift and drag coefficients (C_L and C_D) over the first four flapping cycles at Re = 75.

filament free end ($y^*(t,0) = y(t,0)/l$) is approximated and plotted in Figure 15. It can be seen that the analytical result is indistinguishable from that obtained through the present numerical framework.

In the second case, the simulation of a rigid thin wing flapping in an enclosed domain at Re = 75 is performed, which has been extensively investigated by Eldredge [35] and Vanella et al. [36] using different numerical methods. In this case, the wing undergoes the heaving and pitching motions simultaneously, with the heaving amplitude being 2.8 times its chord length and the pitching amplitude equal to $\pi/2$. And the phase difference between the heaving and pitching motions is set as 0. It can be seen from Figure 16 that the numerical results based on the current numerical framework agree well with the simulation results from the literature [35, 36] when comparing the lift and drag coefficients (C_L and C_D) over the first four flapping periods.

In the third case, a filament with the dimensionless flexibility 0.0015 and mass ratio 1.5 is

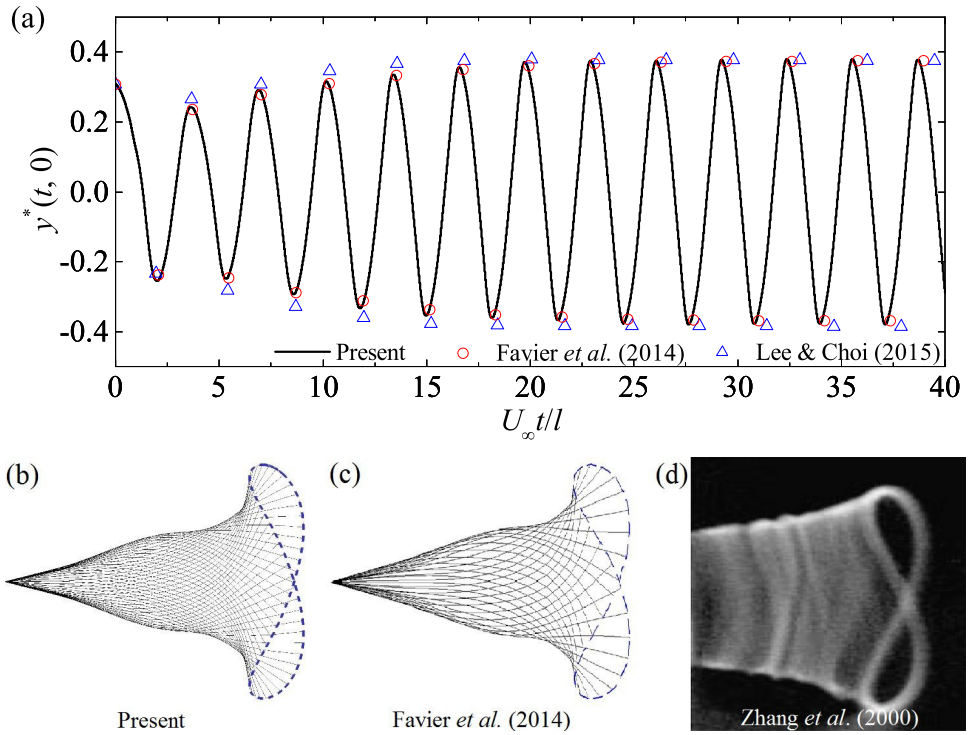

Figure 17: Time histories of the filament's free-end displacement (a) and flapping patterns over one flapping cycle (b) to (d).

immersed in a uniform flow at the filament-length-based Reynolds number, i.e., Re = 200, and it is initially placed at a position angle ($\Theta_0 = \pi/10$) relative to the streamwise direction with the filament boundary conditions the same as in the first case. After released from the rest, the filament undergoes flapping motion under the influence of both the gravitational and flow fields. Figure 17(a) shows that the non-dimensional lateral displacements of the filament free end ($y^*(t, 0) = y(t, 0)/l$) obtained by the current numerical framework agree well with those in the literature [37, 38]. Besides, the periodic flapping pattern of the filament is captured based on the current numerical framework, and is plotted in Figure 17(b). It can be seen that the current flapping pattern well matches that given by Favier et al. [37], as shown in Figure 17(c). Furthermore, the similar flapping pattern is also experimentally discovered by Zhang et al. [39], even though their experiment was conducted at a higher Reynolds number, i.e., Re = $O(10^4)$.

Through the above three validation cases, it can be confirmed that the current numerical framework is well validated. More details of the LBM numerical algorithm and its validation can be found in our previous work [29, 30, 31, 32].

Table 3: Selected cases for convergence test.

Parameter	Values		
	First case	Second case	Third case
Mesh spacing (Δx)	$c/48$	$c/96$	$c/96$
Freestream velocity (U_∞)	$0.02\Delta x/\Delta t$	$0.02\Delta x/\Delta t$	$0.01\Delta x/\Delta t$
Non-dimensional time step ($U_\infty \Delta t/c$)	1/2400	1/4800	1/9600

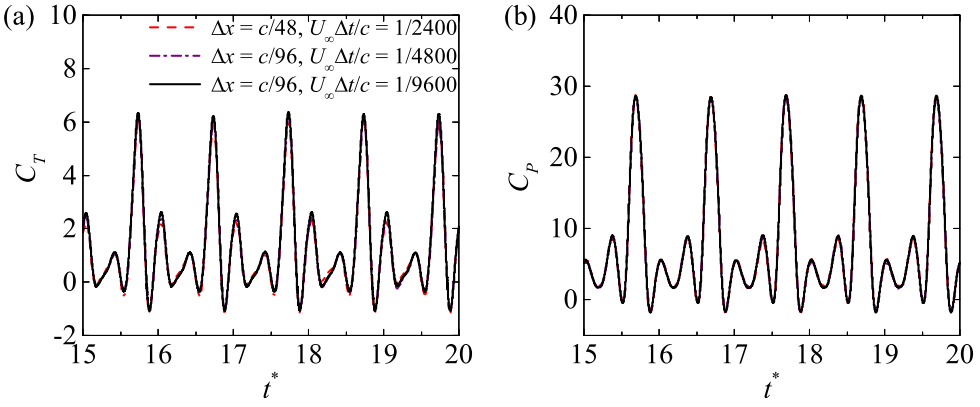

Figure 18: Results for the convergence test: Time histories of the (a) thrust C_T and (b) power coefficients C_P of the heaving flexible foil over five heaving cycles when Re = 200, m^* = 1, EI^* = 4, St = 0.3, $k = \pi/2$ (corresponding to h_b^* = 0.6), f_e^* = 2, h_e^* = 0.15 and $\phi_e = 3\pi/4$. The red dashed, purple dotted-dashed and black solid lines correspond to the cases with $\Delta x = c/48$ and $U_\infty \Delta t/c$ = 1/2400, $\Delta x = c/96$ and $U_\infty \Delta t/c$ = 1/4800, and $\Delta x = c/96$ and $U_\infty \Delta t/c$ = 1/9600, respectively.

A.2 Convergence test

To guarantee the independence of the numerical results in this study on the mesh and time-step resolutions, three cases are selected for the convergence test, as listed in Table 3, where Δt is the unit time step. In these cases, the dimensionless parameters for the fluid and flexible foil are set as Re=200, m^* = 1, EI^* = 4, St = 0.3, $k = \pi/2$ (corresponding to h_b^* = 0.6), f_e^* = 2, h_e^* = 0.15, and $\phi_e = 3\pi/4$. Figure 18 shows that the time histories of the thrust and power coefficients (C_T and C_P) over five heaving cycles for these three cases are nearly indistinguishable. To ensure the accuracy, the mesh and time-step settings for the third case, i.e., $\Delta x = c/96$ and $U_\infty \Delta t/c$ = 1/9600, are adopted throughout this study.

Acknowledgments

We gratefully acknowledge the financial support for this study from the Research Grants Council of Hong Kong under General Research Fund (Project No. 152493/16E) and the Departmental General Research Fund (Project No. G-UA5A & G-YBLP) from the Department of Mechanical Engineering of The Hong Kong Polytechnic University. We also acknowledge Dr Zheng Fan from School of Mechanical and Aerospace Engineering, Nanyang Technological University, for covering some of the computational costs for this study.

References

[1] W. Shyy, Y. S. Lian, J. Tang, D. Viieru, and H. Liu. *Aerodynamics of low Reynolds number flyers*, volume 22. Cambridge University Press, 2007.

[2] C.P. Ellington, C. Van Den Berg, A.P. Willmott, and A.L.R Thomas. Leading-edge vortices in insect flight. *Nature*, 384(6610):626, 1996.

[3] M.H. Dickinson, F.O. Lehmann, and S.P. Sane. Wing rotation and the aerodynamic basis of insect flight. *Science*, 284(5422):1954–1960, 1999.

[4] K. B. Lua, T. T. Lim, K. S. Yeo, and G. Y. Oo. Wake-structure formation of a heaving two-dimensional elliptic airfoil. *AIAA J.*, 45(7):1571, 2007.

[5] J.M. Akkala, A.E. Panah, and J.H.J. Buchholz. Vortex dynamics and performance of flexible and rigid plunging airfoils. *J. Fluids Struct.*, 54:103–121, 2015.

[6] K.B. Lua, S.M. Dash, T.T. Lim, and K.S. Yeo. On the thrust performance of a flapping two-dimensional elliptic airfoil in a forward flight. *J. Fluids Struct.*, 66:91–109, 2016.

[7] S.M. Dash, K.B. Lua, T.T. Lim, and K.S. Yeo. Enhanced thrust performance of a two dimensional elliptic airfoil at high flapping frequency in a forward flight. *J. Fluids Struct.*, 76:37–59, 2018.

[8] J. Tang, D. Viieru, and W. Shyy. Effects of reynolds number and flapping kinematics on hovering aerodynamics. *AIAA J.*, 46(4):967, 2008.

[9] H. Dong, R. Mittal, and F. M. Najjar. Wake topology and hydrodynamic performance of low-aspect-ratio flapping foils. *J. Fluid Mech.*, 566:309–343, 2006.

[10] C.K. Kang, H. Aono, C. E. S. Cesnik, and W. Shyy. Effects of flexibility on the aerodynamic performance of flapping wings. *J. Fluid Mech.*, 689:32–74, 2011.

[11] X.J. Zhu, G.W. He, and X. Zhang. How flexibility affects the wake symmetry properties of a self-propelled plunging foil. *J. Fluid Mech.*, 751:164–183, 2014.

[12] B. Yin and H.X. Luo. Effect of wing inertia on hovering performance of flexible flapping wings. *Phys. Fluids*, 22(11):111902, 2010.

[13] W. Shyy, H. Aono, S. K. Chimakurthi, P. Trizila, C. K. Kang, C. E. S. Cesnik, and H. Liu. Recent progress in flapping wing aerodynamics and aeroelasticity. *Prog. Aerosp. Sci.*, 46 (7):284–327, 2010.

[14] W. Shyy, H. Aono, C.K. Kang, and H. Liu. *An introduction to flapping wing aerodynamics*, volume 37. Cambridge University Press, 2013.

[15] S. Ramananarivo, R. Godoy-Diana, and B. Thiria. Rather than resonance, flapping wing flyers may play on aerodynamics to improve performance. *Proc Natl Acad Sci U S A*, 108 (15):5964–5969, 2011.

[16] H. G. Wu, Y. R. Miyamoto, L. N. G. Castro, B. P. Ölveczky, and M. A. Smith. Temporal structure of motor variability is dynamically regulated and predicts motor learning ability. *Nat. Neurosci.*, 17(2):312–321, 2014.

[17] A. M. Lehn, P. J. M. Thornycroft, G. V. Lauder, and M. C. Leftwich. Effect of input perturbation on the performance and wake dynamics of aquatic propulsion in heaving flexible foils. *Phys. Rev. Fluids*, 2(2):023101, 2017.

[18] A. P. Willmott and C. P. Ellington. The mechanics of flight in the hawkmoth manduca sexta. i. kinematics of hovering and forward flight. *J. Exp. Biol.*, 200(21):2705–2722, 1997.

[19] D. L. Altshuler, W. B. Dickson, J. T. Vance, S. P. Roberts, and M. H. Dickinson. Short-amplitude high-frequency wing strokes determine the aerodynamics of honeybee flight. *Proc. Natl. Acad. Sci. U.S.A.*, 102(50):18213–18218, 2005.

[20] H. Aono, F. Liang, and H. Liu. Near-and far-field aerodynamics in insect hovering flight: an integrated computational study. *J. Exp. Biol.*, 211(2):239–257, 2008.

[21] H. Liu. Integrated modeling of insect flight: from morphology, kinematics to aerodynamics. *J. Comput. Phys.*, 228(2):439–459, 2009.

[22] R. J. Bomphrey, T. Nakata, N. Phillips, and S. M. Walker. Smart wing rotation and trailing-edge vortices enable high frequency mosquito flight. *Nature*, 544(7648):92–95, 2017.

[23] W. X. Huang, S. J. Shin, and H. J. Sung. Simulation of flexible filaments in a uniform flow by the immersed boundary method. *J. Comput. Phys.*, 226(2):2206–2228, 2007.

[24] W. Weaver Jr, S.P. Timoshenko, and D.H. Young. *Vibration problems in engineering*. John Wiley & Sons, 1990.

[25] K. Shoele and Q. Zhu. Performance of a wing with nonuniform flexibility in hovering flight. *Phys. Fluids (1994-present)*, 25(4):041901, 2013.

[26] P. Lallemand and L.S. Luo. Theory of the lattice boltzmann method: Dispersion, dissipation, isotropy, galilean invariance, and stability. *Phys. Rev. E*, 61(6):6546–6562, 2000.

[27] D. Yu, R. Mei, and W. Shyy. A multi-block lattice boltzmann method for viscous fluid flows. *Int. J. Numer. Methods Fluids*, 39(2):99–120, 2002. ISSN 1097-0363.

[28] S. K. Kang. *Immersed boundary methods in the lattice Boltzmann equation for flow simulation*. PhD thesis, Texas A&M University, 2010.

[29] C. Wang, H. Tang, F. Duan, and S.C.M. Yu. Control of wakes and vortex-induced vibrations of a single circular cylinder using synthetic jets. *J. Fluids Struct.*, 60:160–179, 2016.

[30] C. Wang, H. Tang, S.C.M. Yu, and F. Duan. Active control of vortex-induced vibrations of a circular cylinder using windward-suction-leeward-blowing actuation. *Phys. Fluids (1994-present)*, 28(5):053601, 2016.

[31] C. Wang, H. Tang, S.C.M. Yu, and F. Duan. Control of vortex-induced vibration using a pair of synthetic jets: Influence of active lock-on. *Phys. Fluids*, 29(8):083602, 2017.

[32] C. Wang, H. Tang, S.C.M. Yu, and F. Duan. Lock-on of vortex shedding to a pair of synthetic jets with phase difference. *Phys. Rev. Fluids*, 2:104701, Oct 2017. doi: 10.1103/PhysRevFluids.2.104701. URL `https://link.aps.org/doi/10.1103/PhysRevFluids.2.104701`.

[33] S. Izquierdo and N. Fueyo. Characteristic nonreflecting boundary conditions for open boundaries in lattice boltzmann methods. *Phys. Rev. E*, 78(4):046707, 2008.

[34] J.S. Chen, J.Y. Chen, and Y.F. Chou. On the natural frequencies and mode shapes of dragonfly wings. *J. Sound Vib.*, 313(3):643–654, 2008.

[35] J. D. Eldredge. Numerical simulation of the fluid dynamics of 2d rigid body motion with the vortex particle method. *J. Comput. Phys.*, 221(2):626–648, 2007.

[36] M. Vanella, T. Fitzgerald, S. Preidikman, E. Balaras, and B. Balachandran. Influence of flexibility on the aerodynamic performance of a hovering wing. *J. Exp. Biol.*, 212(1): 95–105, 2009.

[37] J. Favier, A. Revell, and A. Pinelli. A lattice boltzmann–immersed boundary method to simulate the fluid interaction with moving and slender flexible objects. *J. Comput. Phys.*, 261:145–161, 2014.

[38] I. Lee and H. Choi. A discrete-forcing immersed boundary method for the fluid–structure interaction of an elastic slender body. *J. Comput. Phys.*, 280:529–546, 2015.

[39] J. Zhang, S. Childress, A. Libchaber, and M. Shelley. Flexible filaments in a flowing soap film as a model for one-dimensional flags in a two-dimensional wind. *Nature*, 408(6814): 835–839, 2000.